

Electronic Supporting Information: Detection of electron tunneling across plasmonic nanoparticle-film junctions using nitrile vibrations

Hao Wang, Kun Yao, John A. Parkhill*, Zachary D. Schultz*

Department of Chemistry and Biochemistry, University of Notre Dame,
Notre Dame, Indiana 46556, United States.

*Email: Schultz.41@nd.edu; john.parkhill@nd.edu

Table of Contents

1. PM-IRRAS and AFM characterization of the MBN on Au film.....	2
2. Estimation of the gap distance in NPoMs.....	3
3. Molecular orbital distributions and charge-transfer energy.	5
5. Symmetry vs. asymmetry of the nitrile stretch.	7
6. Dark field microscopy of NPoMs: single AuNPs vs. aggregates.....	9
7. DFT calculation and Raman peak assignments.	10
8. SERS on clustered NPoMs.....	12
9. Correlation of large stark shifts with new SERS peaks.	13
10. Simulation of nitrile peak evolution under intense local fields.....	14
11. Scattering profiles of single NPoMs.....	15
12. Time dependence of SERS in single isolated NPoM gaps.....	16
13. Peak analysis for the time-dependent SERS spectra.	17
References.....	18

1. PM-IRRAS and AFM characterization of the MBN on Au film.

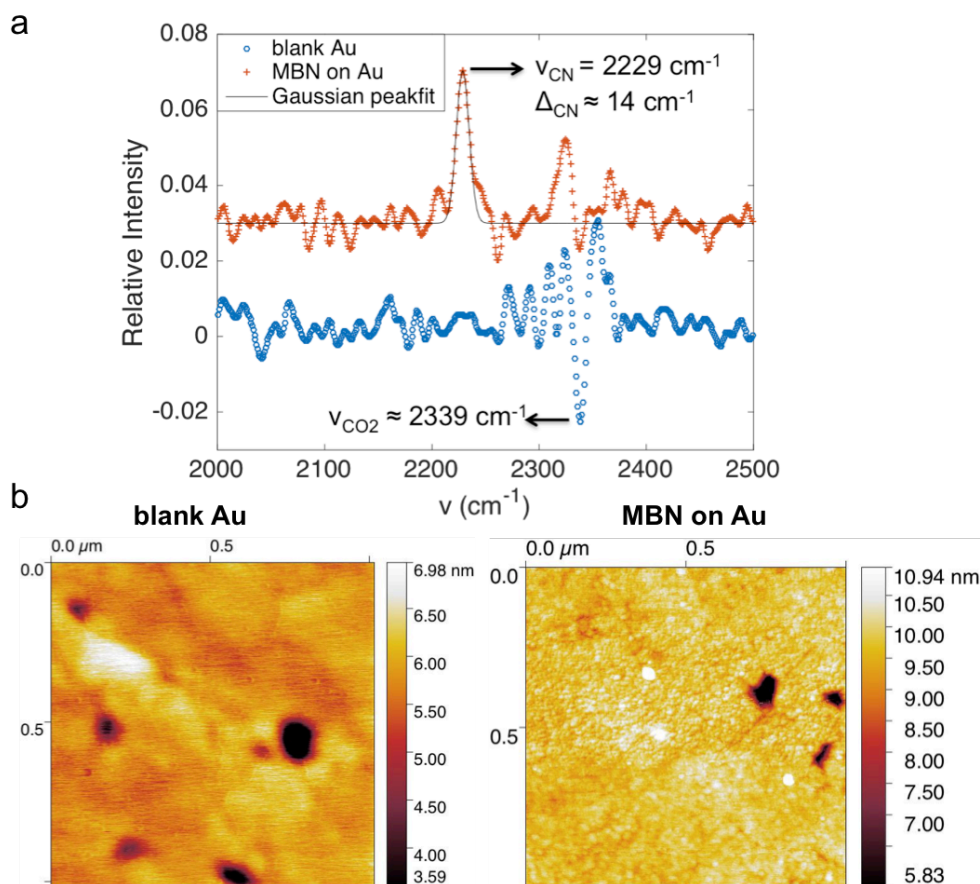


Figure S1. a) The PM-IRRAS spectrum of the mercaptobenzonitrile (MBN) film (red) shows a single peak in the CN stretching area with a frequency of 2229 cm^{-1} and a width of 14 cm^{-1} , that is clearly resolved over the background spectrum of the Au surface (blue). b) The AFM images of the blank and MBN functionalized gold surface (Roughness values, R_q , for blank Au and MBN-Au are 0.46 nm and 0.54 nm , respectively).

Surface IR spectra were taken using PM-IRRAS on a Nicolet iS50R spectrometer (Thermo, Waltham MA). All optical components were purchased from Thorlabs (Newton NJ) unless otherwise specified. The infrared beam was passed from the spectrometer exit port and directed through an $f/7$ KRS-5 lens (Infrared Optical Products, Farmingdale, NY) at a 70° incidence angle using uncoated gold mirrors. Next, the beam entered a holographic BaF₂ linear polarizer set at an angle of 45° relative to the optical axis of a Hinds Series II ZNS50 photoelastic modulator (Hinds Instruments, Portland OR), which modulated the beam at a 50 kHz frequency and a half wave retardation of 2500 cm^{-1} . The beam was then focused onto the sample and reflected through a second BaF₂ linear polarizer, which was adjusted to minimize the polarization effects of the substrate. Finally, the light was focused through a BaF₂ lens onto a HgCdTe high D* detector (Thermo, Waltham MA). Spectra were acquired at 8 cm^{-1} resolution and processed using baseline correction and peak fitting packages using Origin Pro software. The AFM images of our gold substrates were acquired on a Digital Instruments Nanoscope V Multimode Scanning Probe Microscope (Bruker, Billerica, MA). Images were processed using Gwyddion software.

2. Estimation of the gap distance in NPoMs.

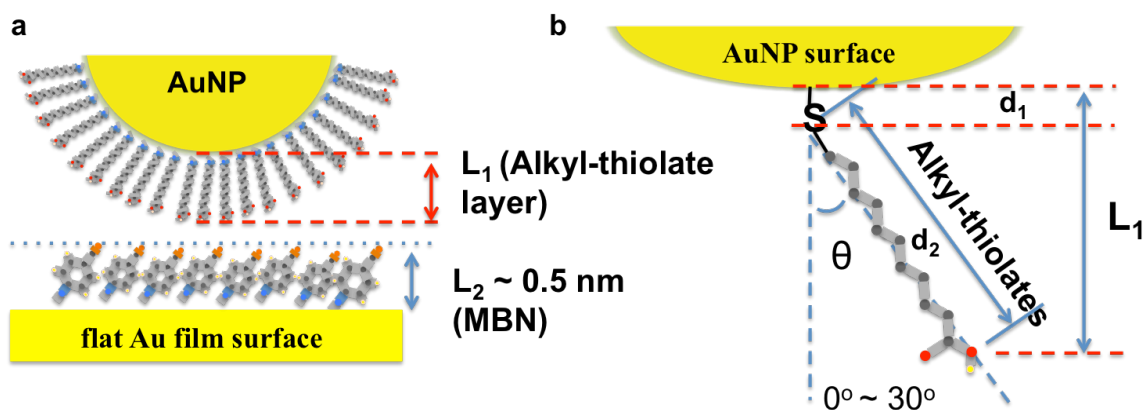


Figure S2. Schematic illustration of the nanoparticle on film (NPoM) structure and the gap distance defined by self assembled monolayers of alkylthiols. (a) Gap distance in between the NPoM junction composed of the MBN molecular monolayer on the flat gold film and the alkyl-thiolate layer assembled on the AuNP surface. (b) Illustration of the alkyl-thiolate monolayer on the AuNP surface. (Red represents oxygen atom, black carbon atom, yellow hydrogen atom)

Table S1. Calculated thickness of the alkyl-thiolate SAM on the gold nanoparticle

		Units: nm		
	Length (d_2)	L_1 (0°)	L_1 (30°)	L_1
TGA (C2)	0.40	0.55	0.50	~ 0.50
MHA (C6)	0.89	1.04	0.92	~ 1.00
MUA (C11)	1.51	1.66	1.46	~ 1.60

TGA: thiolglycolic acid; MHA: mercaptohexanoic acid; MUA: mercaptoundecanoic acid.

The gap distance between gold nanoparticle and gold thin film is controlled by the thickness of two SAMs: the alkyl-thiolate SAM on the gold nanoparticle and the MBN SAM on the flat Au film (Fig. S2a). We estimate the thickness of the alkyl-thiolate monolayer on the surface of the gold nanoparticle using 3D chemical modeling program (Chem3D 15.1). As illustrated in Figure S2b, the alkyl-thiolate molecule (TGA, MHA or MUA) is self-assembled on the gold nanoparticle surface through the formation of Au-S bonds. The tilt angle relative to the nanoparticle surface varies depending the functional groups situated at the distal ends that induce a difference in surface packing density. Here for the alkyl-thiolate monolayer, we assumed a tilt angle of 0° to 30° , as most alkyl-thiolate monolayers are shown to accept some degree of tilt in the formation of densely packed layer¹. The alkyl-thiolate monolayer thickness (L_1) can then be calculated as the height from the gold atom (nanoparticle surface) to the most distant oxygen atom of the alkyl-thiolate. The lengths of the alkyl-thiolate molecules (d_2) were calculated using Chem3D with the consideration of an Au-S bond of 0.15 nm (d_1). The calculated alkyl-thiolate thickness (L_1) is presented in Table S2. In contrast to the well-studied alkyl-thiolate SAMs, reports on the thickness of aromatic SAMs on flat gold films are sparse and often inconsistent across different measuring approaches. Ellipsometry, for example, was used to measure the thickness of thiophenol and 4-methoxy benzyl-mercaptan SAMs

and obtained a value of 0.13 and 0.16 nm, respectively². Meanwhile, using XPS, thiophenol SAM was also reported to be 0.6-0.8 nm.³ Moreover, these measurements are intrinsically ensemble, indirect methods for determining thickness and therefore limited by the uncertainty of various parameters such as the index of refraction, surface contamination, etc. The most reliable experimental data for these aromatic-thiolate SAMs comes from direct measurement of the SAM thickness, such as high resolution STEM (HR-STEM). In our paper, we adopted a thickness (L_2) of 0.5 nm for the MBN SAM based on a value determined for benzene-dithiol (BDT) SAM using HR-STEM.⁴ Using Chem3D, the theoretical length of MBN (0.61 nm) is very close to that of the BDT (0.60 nm) assuming a tilt angle of 30°. We further checked the validity of the thickness values by comparing them to previously calculations and/or experimental values for the alkyl-thiolate SAMs. Our estimation of the thickness of the alkyl-thiolate agrees with those computed by Hill et al.⁵ and those experimentally determined by Bain et al.¹ Therefore, we believe our estimated gap junction sizes (~1.0 nm, ~1.5 nm and ~2.1 nm, for AuNP@TGA NPoM, AuNP@MHA NPoM and AuNP@MUA NPoM, respectively) provide a reasonable approximation of the gap distances within the NPoM systems.

3. Molecular orbital distributions and charge-transfer energy.

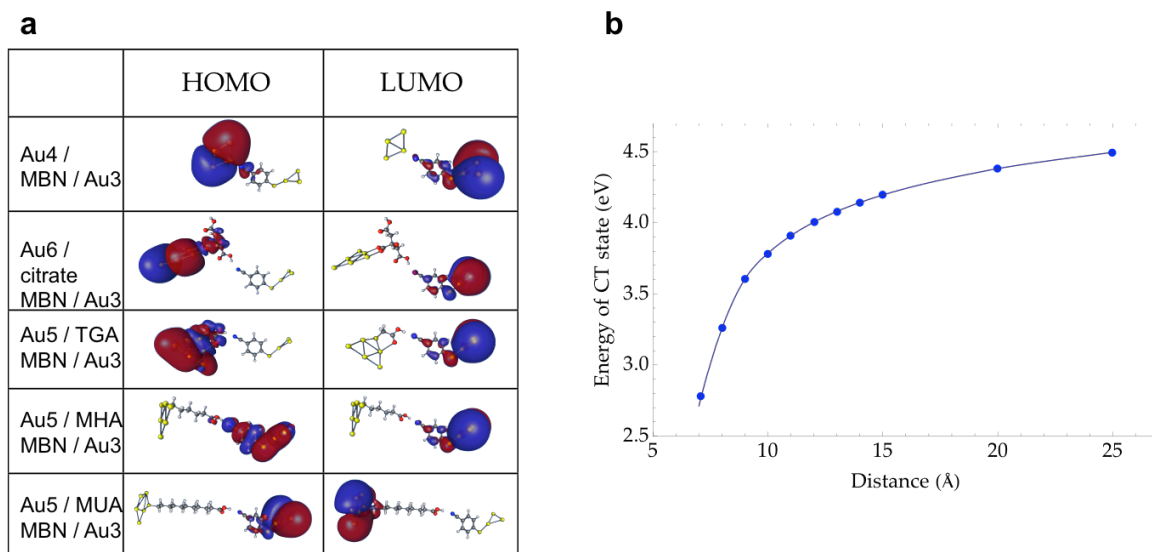


Figure S3. (a) Calculated HOMO and LUMO orbital distributions on the Au4 / MBN / Au3 clusters with different ligands used to simulate the experimental nanostructures. (b) Energy required for the charge transfer process with varying gap distances (defined as the distance between Au4 and Au3).

DFT calculation shows that the HOMO orbital stays is on the AuNP and the LUMO lies on the Au-film when no ligand is attached to the Au4 or with short ligands such as citrate and TGA absorbed to AuNP. This means that charge transfer from HOMO and LUMO can occur with the ligand on the AuNP and subsequently lead to the charge-state induced large peak shift. In contrast, when AuNP is bonded with MHA or MUA, the positions of the HOMO or LUMO orbitals changes and the electron transfer process is more challenging. Furthermore, the calculated charge-transfer energy of varying gap distances follows a steeper decay as the gap size decreases. This also agrees well with our experimental observation that only in very small gaps (≤ 1 nm) are the molecular-charging induced lower-energy peaks observed.

4. Spatial distributions of the high & low-energy nitrile peaks.

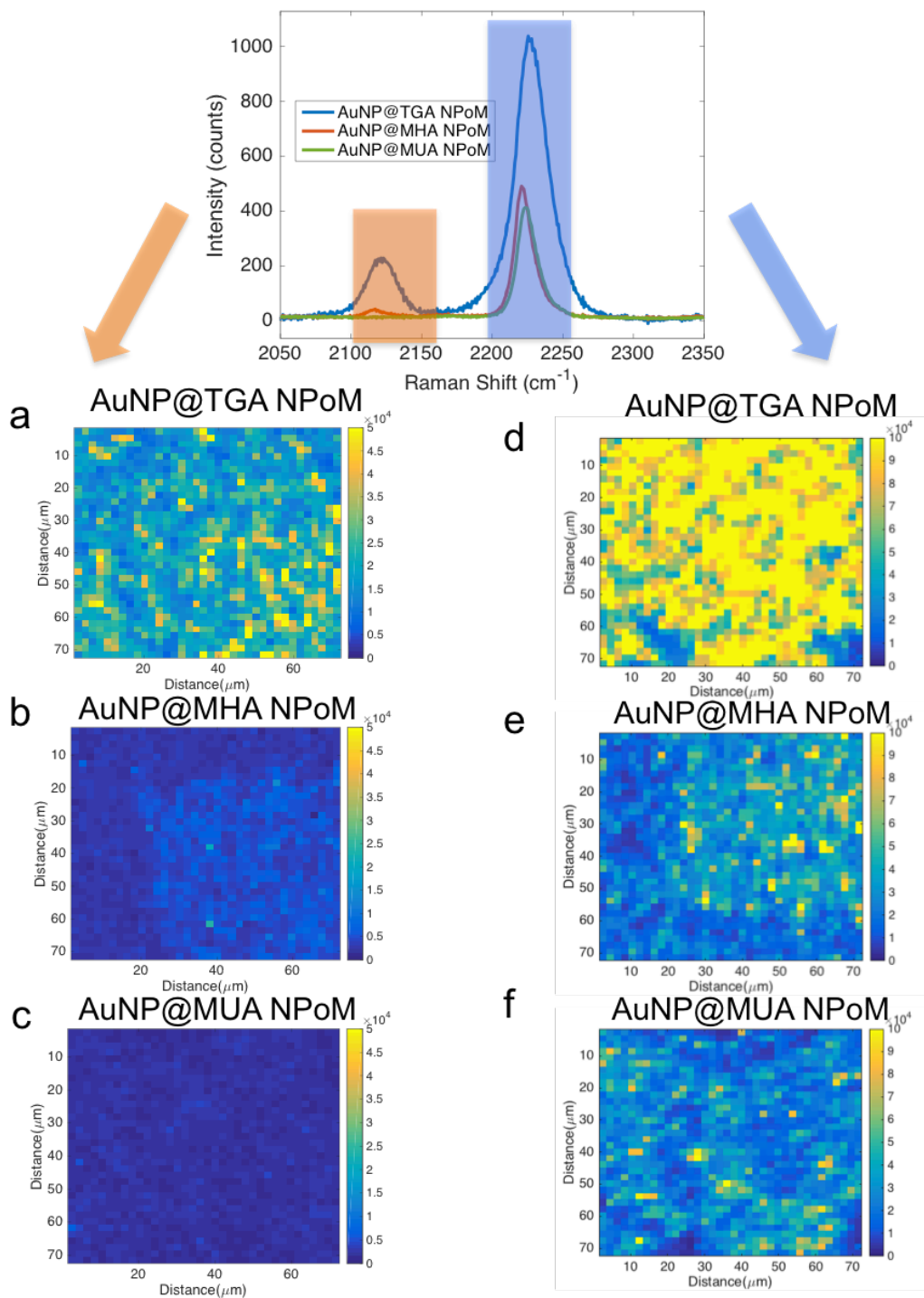


Figure S4. SERS intensity maps for three different NPoM systems: (a, d) AuNP@TGA, (b, e) AuNP@MHA, and (c, f) AuNP@MUA absorbed onto the MBN modified gold films (area $\sim 70 \times 70 \mu\text{m}^2$), integrated at the $\sim 2125 \text{ cm}^{-1}$ band (orange shaded region) shown on the left column (a, b, c) and the $\sim 2223 \text{ cm}^{-1}$ band (blue shaded region) on the right (d, e, f), respectively. The figures (d, e, f) are the same as Figure 2a-c and used as comparison here. The color scales were normalized for the 2125 cm^{-1} and 2223 cm^{-1} bands separately for clarity.

5. Symmetry vs. asymmetry of the nitrile stretch.

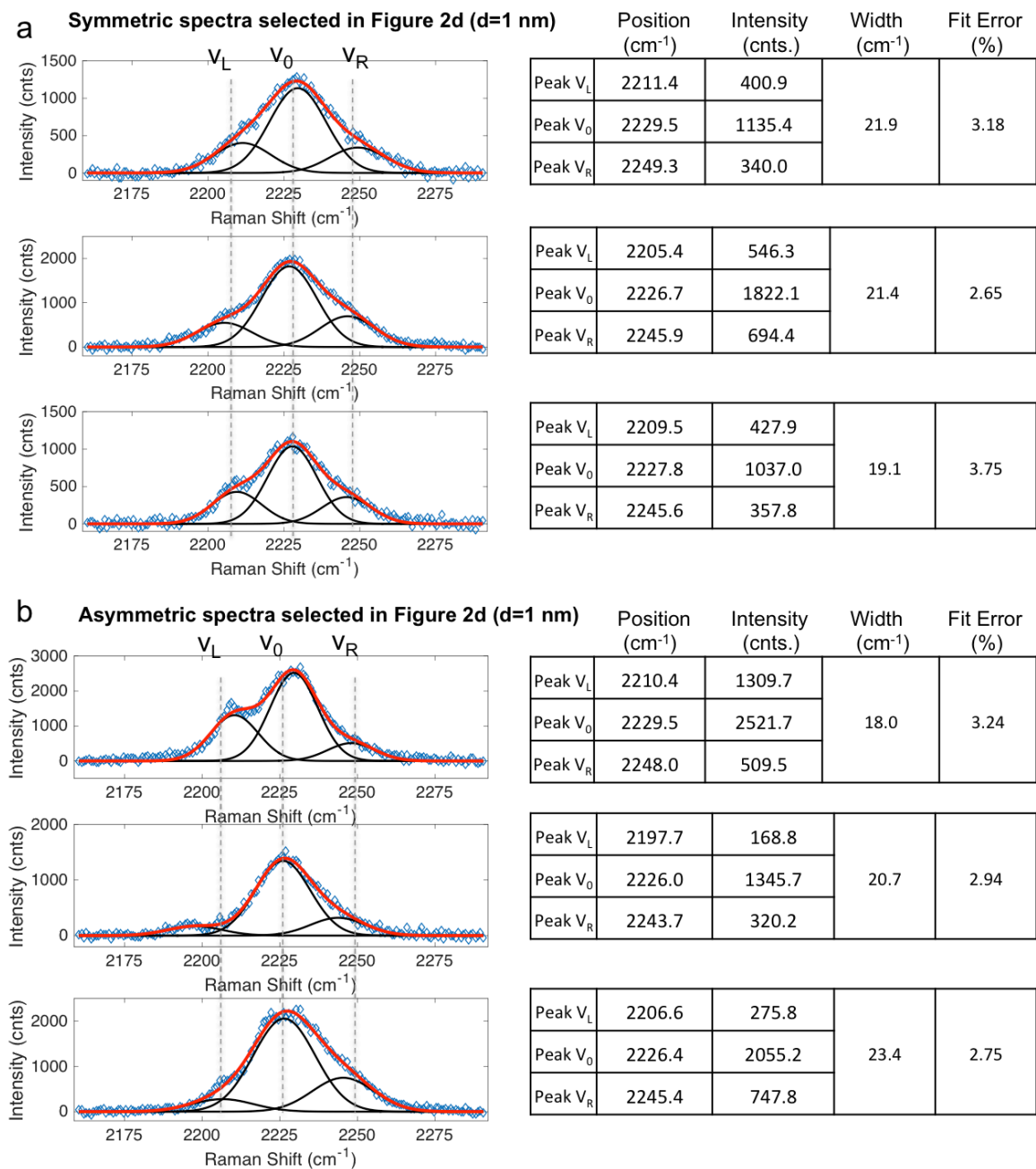
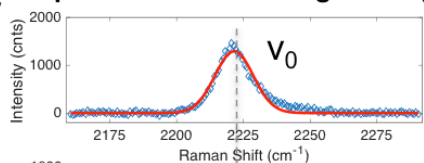
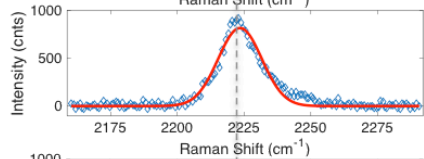


Figure S5. Examples of the symmetrically (a) and asymmetrically (b) broadened SERS nitrile spectra as selected from Figure 2d (AuNP@TGA NPoMs) and the fitted peak parameters. The black curves are the deconvoluted Gaussian components that contribute to the total lineshape (red curve). ν_0 is the isotropic nitrile stretch; ν_L and ν_R are the red-shifted and blue-shifted nitrile stretch, respectively. Dotted lines are provided as guides to the eye.

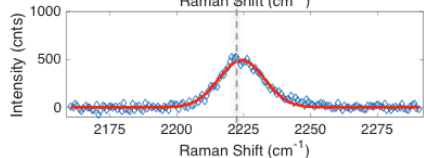
C Spectra selected in Figure 2e (d=1.5 nm)



	Position (cm ⁻¹)	Intensity (cnts.)	Width (cm ⁻¹)	Fit Error (%)
Peak V ₀	2221.5	1292.1	16.9	4.16

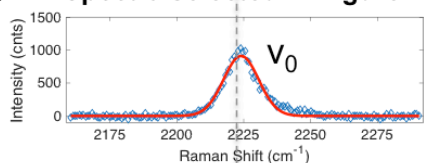


Peak V ₀	2223.5	816.7	19.2	5.10
---------------------	--------	-------	------	------

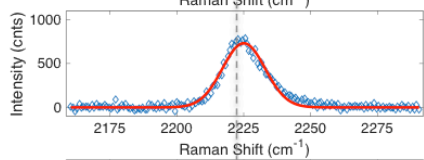


Peak V ₀	2224.2	490.9	20.1	5.18
---------------------	--------	-------	------	------

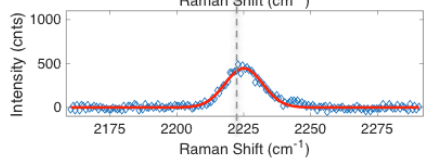
d Spectra selected in Figure 2f (d=2.1 nm)



	Position (cm ⁻¹)	Intensity (cnts.)	Width (cm ⁻¹)	Fit Error (%)
Peak V ₀	2224.0	911.9	15.5	3.90



Peak V ₀	2225.0	731.5	18.8	4.68
---------------------	--------	-------	------	------



Peak V ₀	2225.0	445.7	16.6	5.14
---------------------	--------	-------	------	------

Figure S5c-d. Examples of the symmetrical nitrile SERS spectra as selected from Figure 2e (AuNP@MHA NPoMs) and 2f (AuNP@MUA NPoMs) and the corresponding fitted peak parameters. These nitriles bands can be adequately fitted with a single Gaussian function (red curve). ν_0 is the isotropic nitrile stretch and the dotted lines are provided as guides to the eye.

6. Dark field microscopy of NPoMs: single AuNPs vs. aggregates.

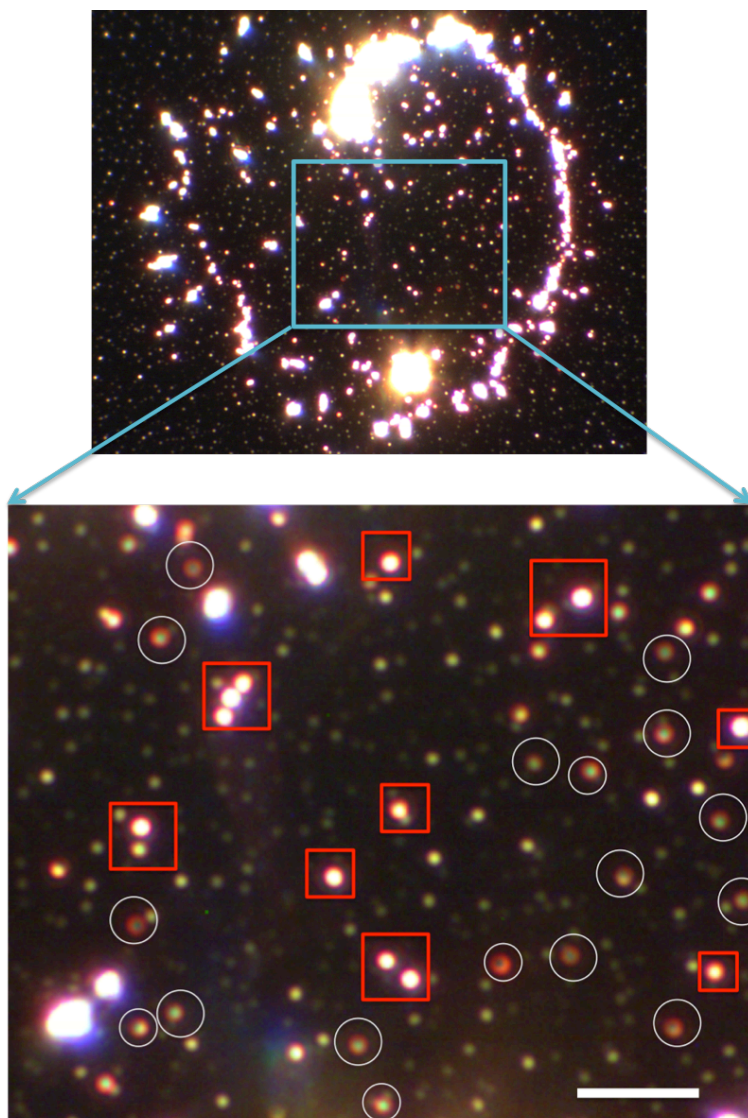


Figure S6. True-color dark-field microscopic (100x, NA=0.9, DF) image of AuNP@TGA NPoMs. The red squares represent aggregated AuNPs on the MBN covered gold film. The white circles represent those single isolated AuNPs later used for plasmon resonance and SERS analysis. (Scale bar is 5 μm)

AuNPs physisorbed onto the MBN functionalized gold film often produce a mixture of nanoparticle clusters. Due to the “coffee ring effect”, drop-casted AuNPs tend to form large aggregates on the outer “ring” and scatter much brighter than smaller assemblies. Near the center of the ring, single isolated AuNPs on gold film can be identified as those with a characteristic red “doughnut” pattern (white circles), whereas multi-particle assemblies on the gold film were identified as those with a bright-scattering center (red squares). The distinct scattering patterns for single AuNP NPoMs and clustered NPoMs have been reported in previous publications⁵ and can be used to distinguish single AuNP NPoMs from those aggregated AuNP NPoMs that involve contributions from inter-particle couplings.

7. DFT calculation and Raman peak assignments.

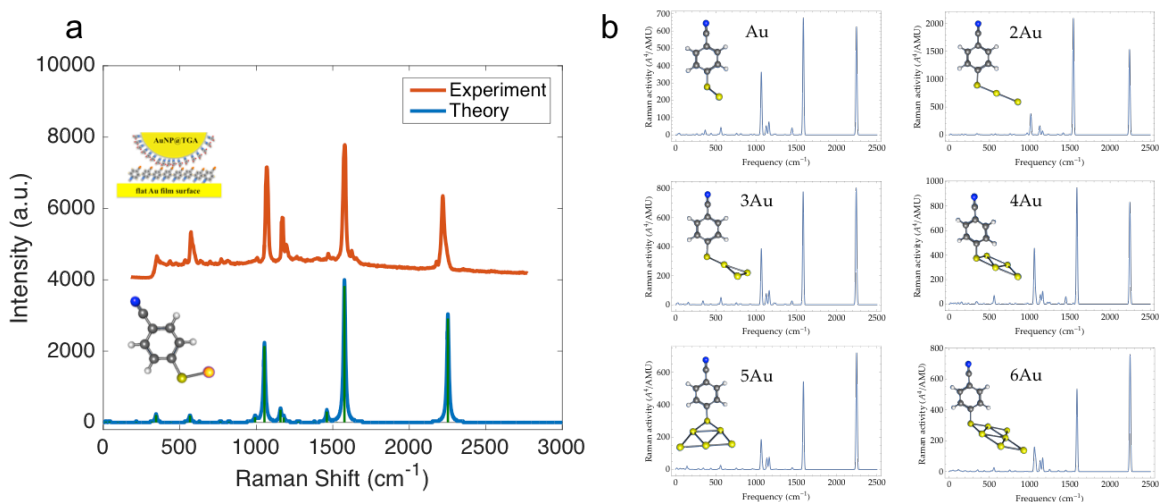


Figure S7. Experimental SERS spectrum of MBN (red curve) obtained from a typical NPoM system compared with the DFT calculated Raman spectrum of the MBN-Au adduct (a). Theoretical spectrum was modeled using a Lorentzian function (fwhm=8 cm⁻¹) and offset for better comparison with the experimental one. The major Raman peaks of the MBN were found to be relatively unchanged by different numbers of the Au atoms used in the calculation (b).

DFT calculations were performed with the hybrid exchange functional of ω B97X. The geometry was optimized and then used to calculate the Raman spectrum.⁶ The basis sets for C, N, S and H were 6-31G** with polarization functions for C, N, S and H, and diffuse function only for C, N and S atoms. For the gold atom, the valence and core electrons were described by the LanL2DZ basis set and the corresponding relativistic effective core potential (ECP).⁷ The DFT calculation was carried out using Q-Chem 4.2 package. All calculated vibrational frequencies were corrected by a scaling factor of 0.93 to account for the approximations made for describing the potential energy surface and calculating the electronic structure and interactions. The Intensities of the Raman bands were estimated by calculating the differential Raman cross sections of each mode. An excellent agreement of the experimental SERS result and the theoretical Raman spectrum of the MBN-Au complex can be found in Fig. S7a. Therefore, prominent SERS peaks were subsequently assigned based on the DFT calculation and the corresponding modes were listed in Table S2. Not surprisingly, the SERS modes are dominated by the benzene ring modes and CN stretching mode of the MBN molecule residing in the gap, whereas the alkylthiolate signals were negligible due to its much smaller Raman cross section. We also verified the effect of Au atoms on the DFT calculation. As shown in Fig. S6b, the number of Au atoms does not significantly change the Raman peak positions of the MBN molecule.

Table S2. SERS peak assignment based on DFT calculation

DFT Calculation		SERS Experiment		Vibrational Modes
Position (cm ⁻¹)	Norm. Intensity (Å ⁴ /AMU)	Position (cm ⁻¹)	Intensity (counts)	
564	0.05	574	1341	Skeletal breath, C-S, C-C
1054	0.56	1069	3159	Ring breath C-H, C-C
1160	0.10	1170	1745	Ring C-H
1576	1.00	1578	3784	Ring stretch C-H, C-C
2252	0.76	2219	2353	CN stretch

8. SERS on clustered NPoMs.

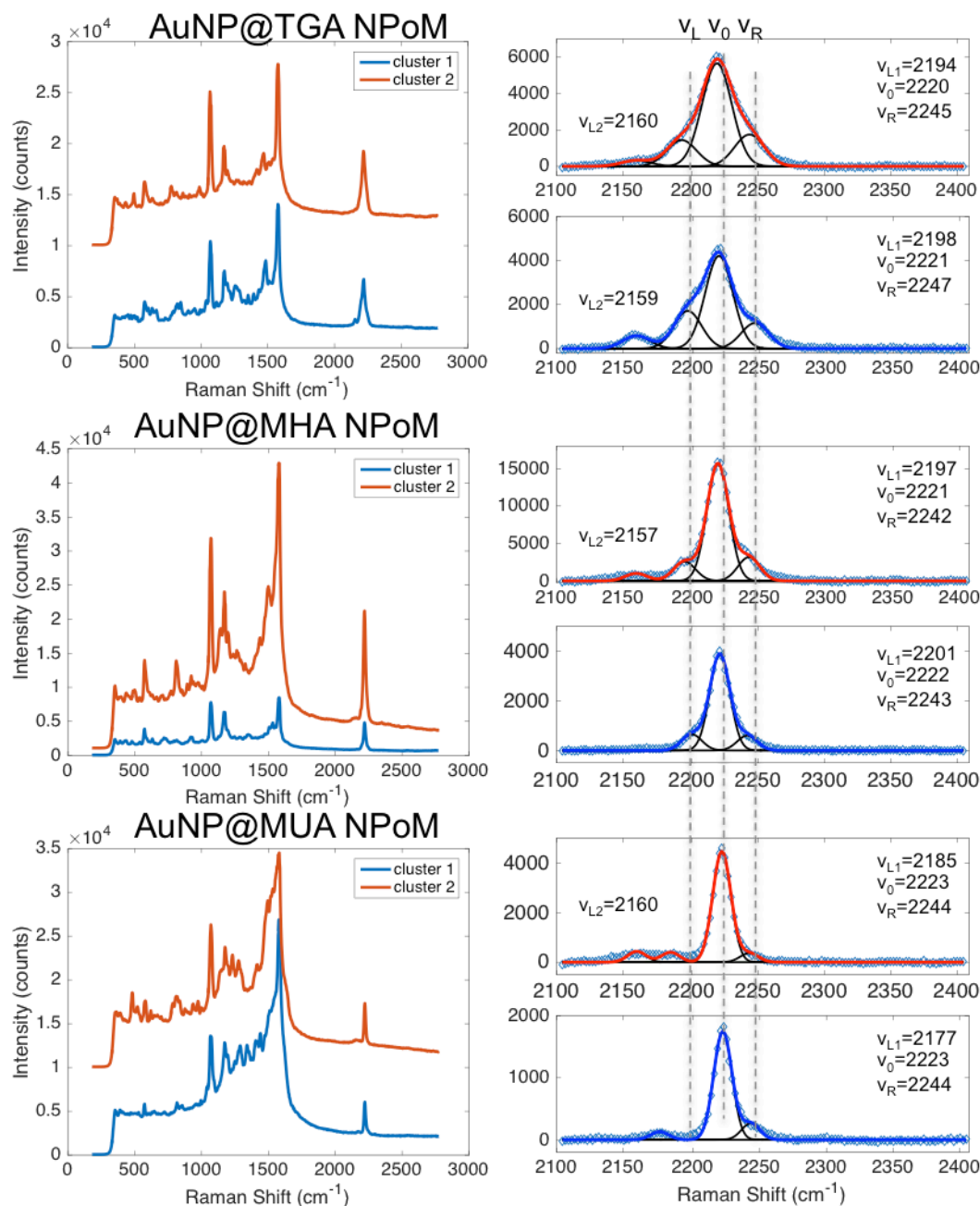


Figure S8. SERS of clustered NPoMs. The panel on the left shows the acquired SERS spectra from each different type of NPoMs and on the right show the corresponding nitrile SERS bands resolved into multiple shifted components. SERS spectra were offset for comparison and the dotted lines are guides for the eye.

Local electric field within metal nanostructures is known to be highly dependent on the near-field plasmonic coupling effect, which differs significantly for isolated single nanoparticles on the gold film and clustered nanoparticle assembled on the gold film. In clustered assemblies, particle-film gap size is no longer the single most important factor that determines plasmonic coupling and the strength of the resulting local electric fields. Inter-particle coupling, as demonstrated by Tian et al.,⁸ can also severely affect and

contribute to the enhancement of the local electric fields in the particle-film gap. In Figure S7, we show that peak shifts were observed for all types of clustered NPoMs, regardless of the length of the alkylthiolate ligands. This stands in contrast to the trend observed in isolated single AuNPs on the gold film, where peak shifts were absent for NPoMs with larger gap sizes, e.g. AuNP@MHA NPoMs and AuNP@MUA NPoMs (See Figure 5). In most clustered NPoMs, a blue shift and a red shift in the range of $(\pm 21 \text{ cm}^{-1}) \sim (\pm 26 \text{ cm}^{-1})$ were routinely observed regardless of the gap sizes (Fig. S7). Further red shifted peaks were observed to appear at $\sim 2160\text{-}2177 \text{ cm}^{-1}$. On the basis of vibrational stark effect, the observed redshift of $(-46 \text{ cm}^{-1}) \sim (-63 \text{ cm}^{-1})$ suggests an even higher local electric field ($> 70 \text{ MV/cm}$) for these clustered NPoMs, where field ionization can initiate photoreactions. Interestingly, it does appear, comparing the SERS spectra obtained from single NPoMs and clustered NPoMs, that spurious Raman signals likely associated with photoproducts increases along with the appearance of the abnormally large stark shifts (Fig. S8).

9. Correlation of large stark shifts with new SERS peaks.

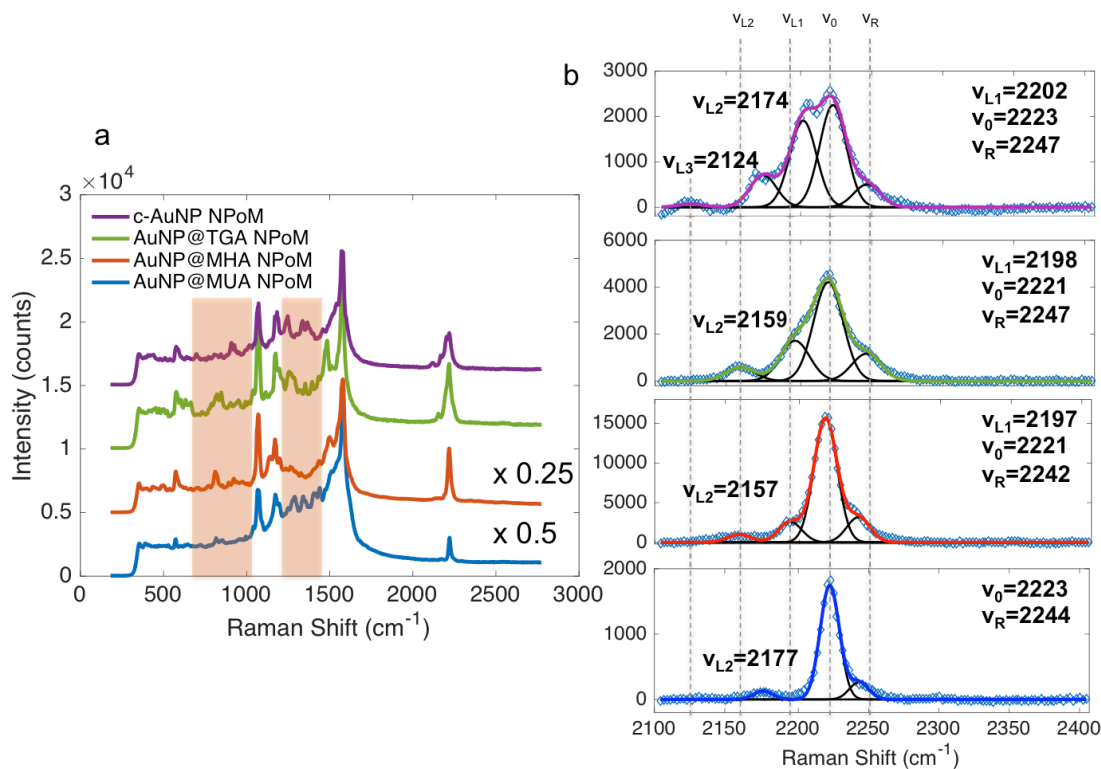


Figure S9. Comparison of SERS signals acquired in different types of clustered NPoMs. (a) SERS spectra from various clustered NPoM systems. The shaded region shows some spurious SERS peaks that cannot be assigned to MBN directly. (b) Nitrile SERS bands resolved into multiple shifted components. The spectra were offset for comparison and the dotted lines are guides for the eye.

Here we compiled representative SERS responses from various clustered NPoMs and demonstrate the correlation between the large stark shifts observed ($50\text{-}60 \text{ cm}^{-1}$) and the emergence of some SERS bands that cannot be directly assigned to MBN. These bands clearly differentiate themselves from MBN normal modes attributed in Figure S6

and Table S2. The source of these vibrational modes (shaded regions in Figure S8) are most likely the photoproducts formed in these gaps due to the extremely intense local electric fields and the resulting field ionization, similar to those observed previously in studying photochemical processes of molecules under ultra-high electric fields with a SERS substrate.⁹ The further red shifted peaks located at $\sim 2157\text{-}2177\text{ cm}^{-1}$ correspond to local electric fields with the magnitude of $75\text{-}105\text{ MV/cm}$, which is close to or above the typical electric field threshold for photodamage ($1\text{-}10\text{ GV/m}$).⁹

10. Simulation of nitrile peak evolution under intense local fields.

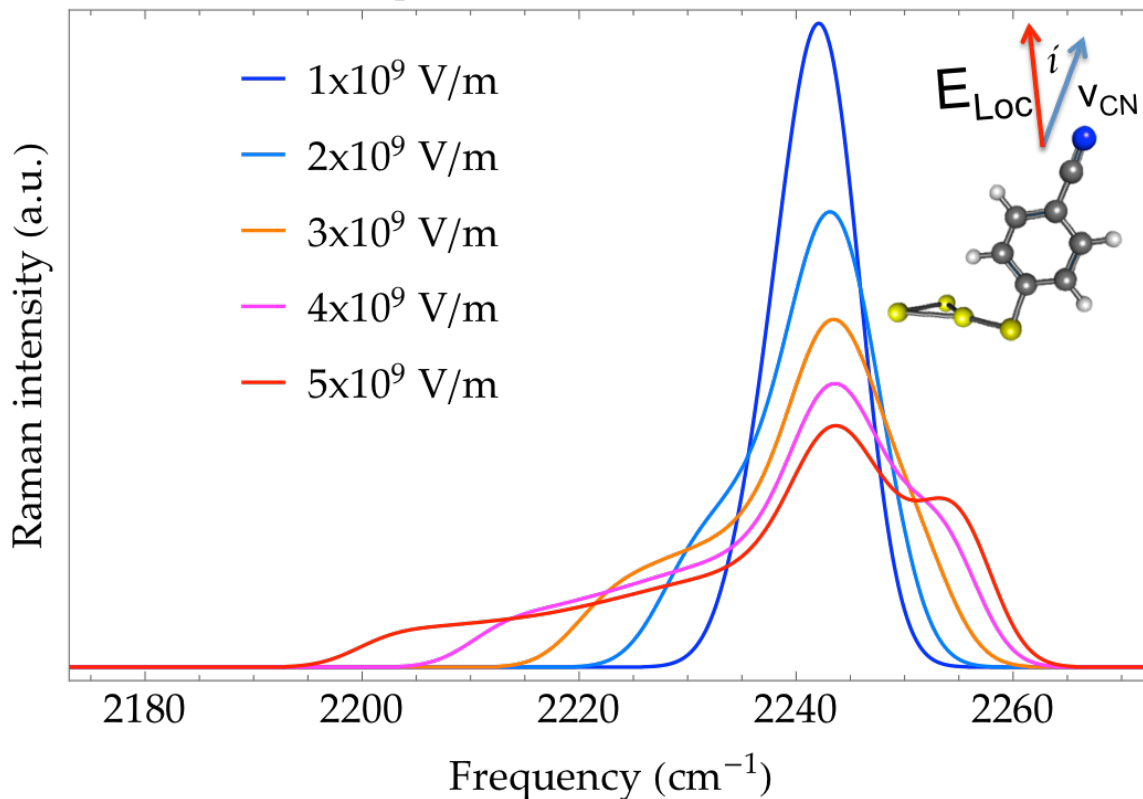


Figure S10. Simulated line-shape evolution for the nitrile vibration with oscillating electric fields of various magnitudes. The maximum local field strength (E_m) increases from 1×10^9 to 5×10^9 V/m.

To simulate the evolution in line-shape of the nitrile vibration under intense local electric fields, we developed a model where the oscillating nature of the local fields is accounted for. The local electric field is defined as an optical fields $E_{Loc} = E_m \cdot \cos[(2\pi/100) \cdot t]$; $t = [0, 100]$. We then have an effective local field component that is projected on the dipole of the vibrational mode: $E_{eff} = E_{Loc} \cdot \cos[(\pi/100) \cdot i]$; $i = [0, 100]$. If each effective local field component corresponding to a specific peak shift as presented in Fig. 4c can be integrated, we then obtain a peak-shape evolution as E_m increases shown in Fig. S9, and clearly the asymmetry of the nitrile peak become obvious under highly intense local electric fields. This qualitatively agrees with our experimental observation in single and clustered NPOMs.

11. Scattering profiles of single NPoMs.

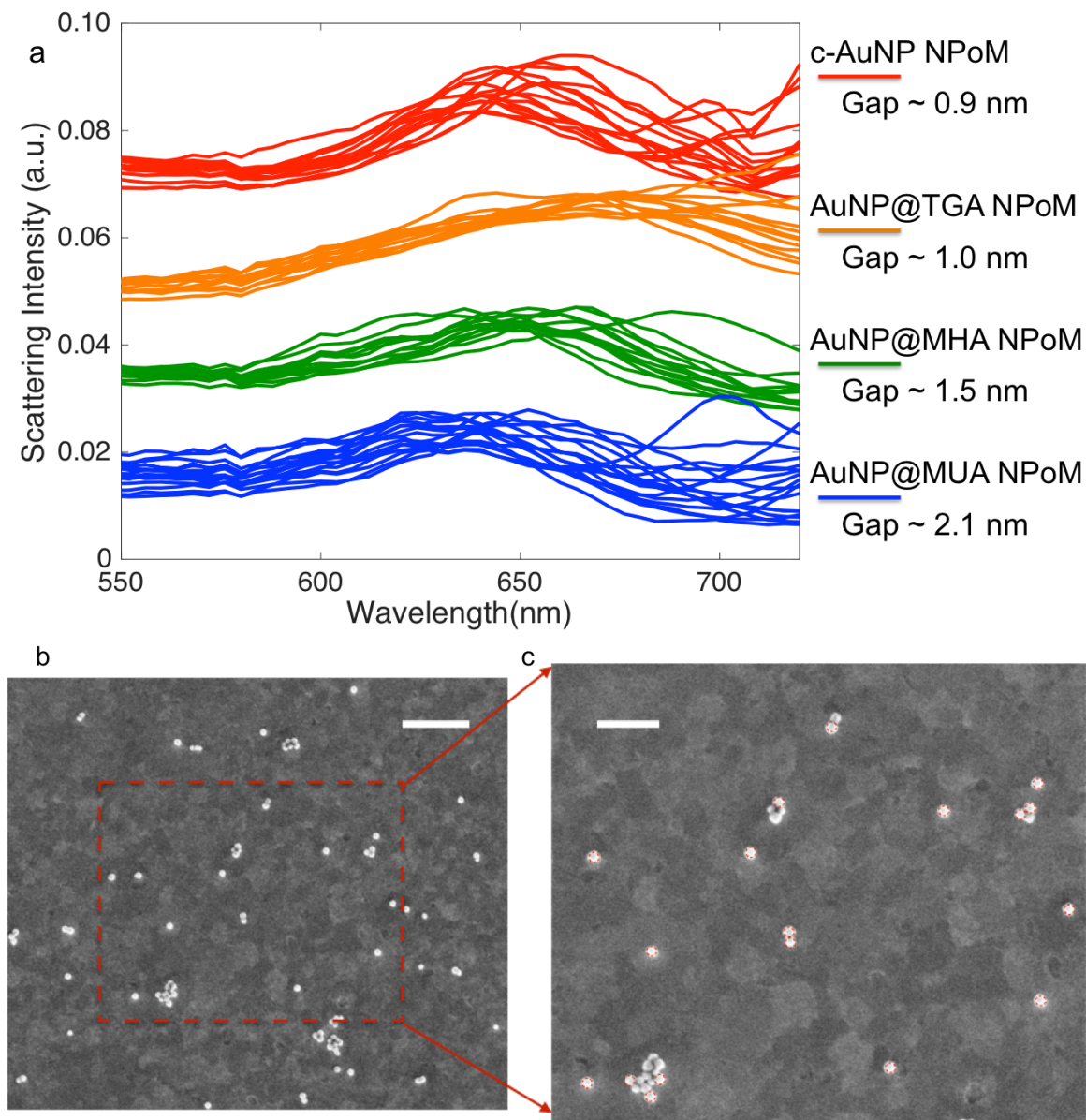


Figure S11. (a) Dark-field scattering profiles from different NPoM systems. Small variations in the center of the plasmon resonances were observed across samples. The scattering intensities were normalized and offset for comparison. (b, c) Typical SEM images of 80nm AuNP@TGA NPoMs prepared with a good size distribution even though small variations in size and shape of the AuNPs do exist. (Scale bar is 1 μm in b and 500 nm in c)

Characterizing the scattering resonances from the coupled plasmon modes in small gaps is of great importance in understanding the local field enhancement and electronic processes such as charge tunneling. To correlate the stark shifts observed in SERS with the local plasmon resonances, we further measured the dark-field scattering properties of these single NPoMs. The scattering resonances continuously red shift from ~ 640 nm, ~ 647 nm, to ~ 671 nm when the gap distances decrease from 2.1 nm to 1.5 nm to 1.0 nm. However, when the gap size goes below 1 nm, the trend reversed and a blue

shift was observed. The onset value of the quantum regime where blue shift takes place is larger than those reported for through-space quantum tunneling (below 0.5 nm) and close to those reported for through-bond tunneling (~ 1 nm).

12. Time dependence of SERS in single isolated NPoM gaps.

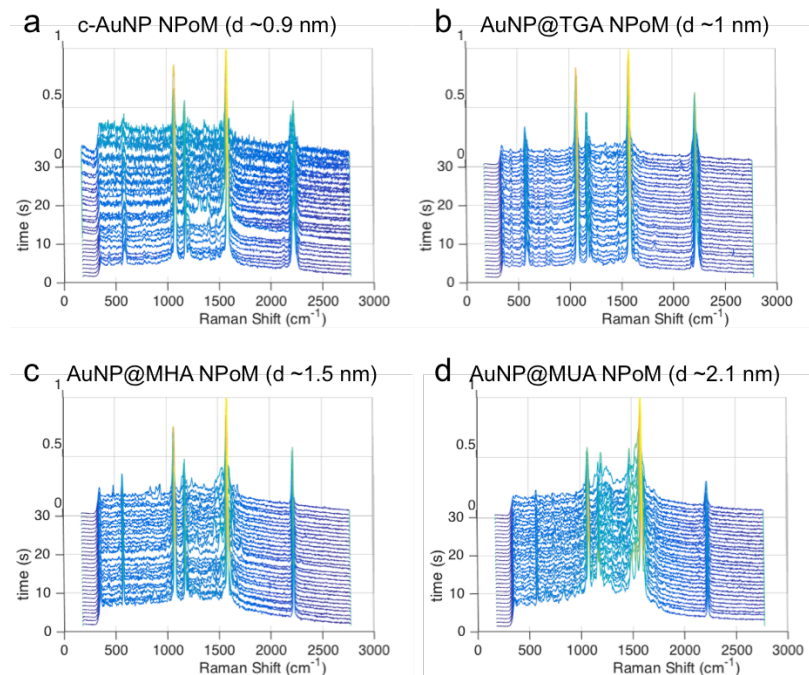


Figure S12. Full spectral evolution in various single NPoM systems within a time frame of 30s, 1s per acquisition. The SERS intensities were normalized to the highest peak in each spectrum.

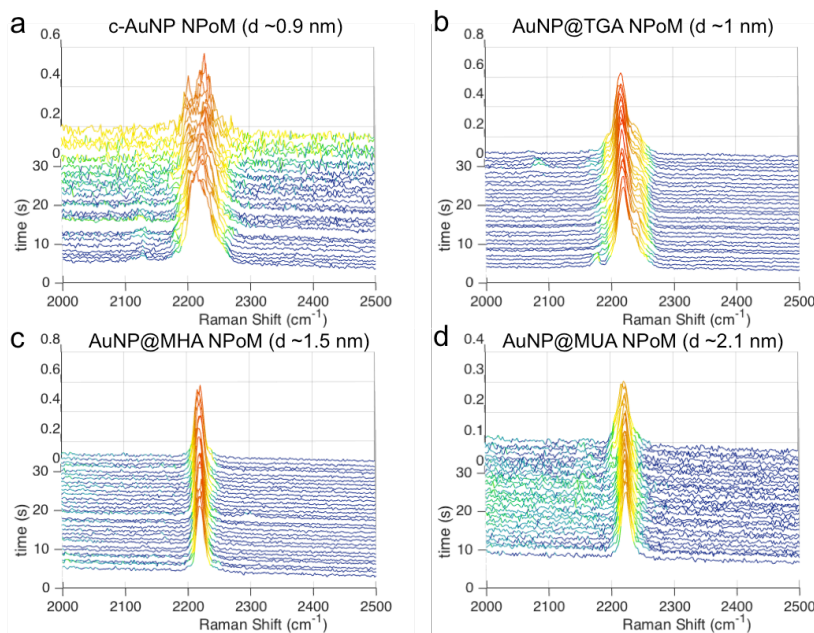


Figure S12. The same plot as above but zoomed in the nitrile stretch region in order to see the details.

13. Peak analysis for the time-dependent SERS spectra.

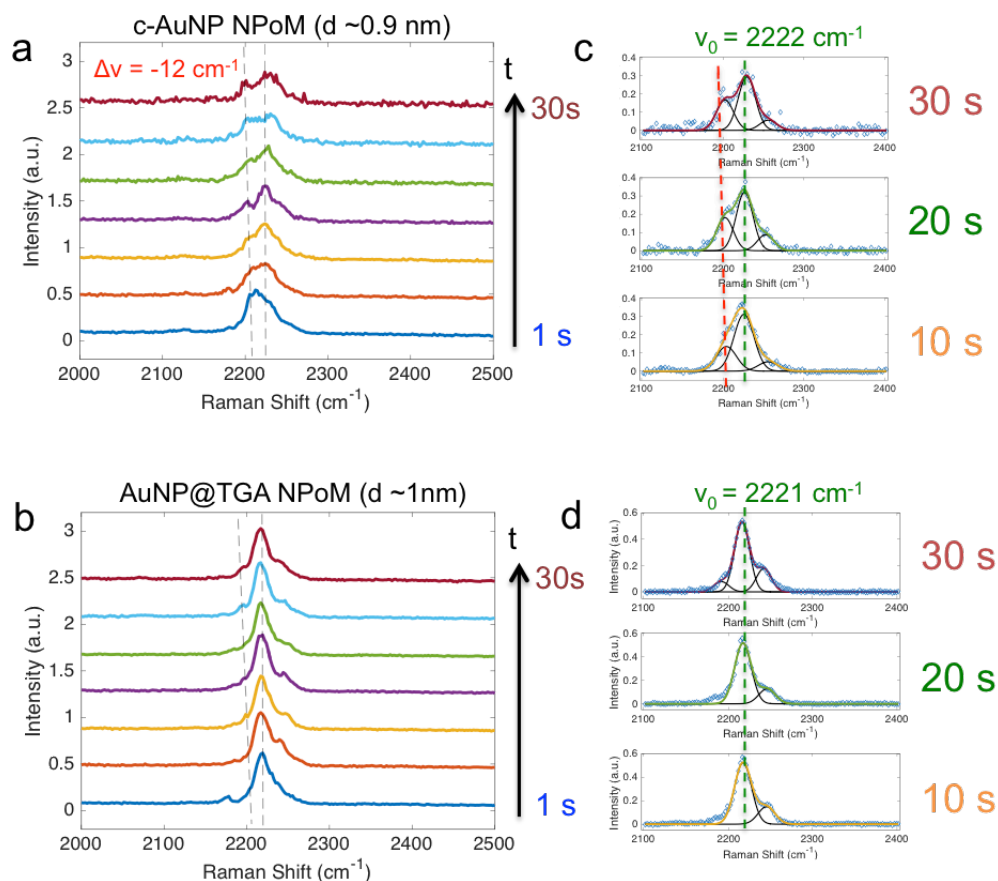


Figure S13. (a, b) SERS spectra selected from the time series (1s, 5s, 10s, 15s, 20s, 25s, 30s) of smaller NPoM gaps. (c, d) corresponding peak fits for selected time points. Dotted lines are guides for the eye.

From the frequency shift observed in the nitrile vibrations, we can obtain a rough estimate of the number of electrons transferred from the AuNP to the flat Au film based on a capacitance model developed by Majima et al.¹⁰ For a charged sphere positioned at a distance ($d \sim 0.9 \text{ nm}$) above a conducting substrate, when the ratio of the gap distance versus the radius of the sphere (d/R) is close to 0, capacitance C can be approximated by $3 \cdot (4\pi\epsilon R)$. Based on the relation: $\Delta V = \Delta E \cdot d = (\Delta v / \Delta \mu_{\text{CN}}) \cdot d = (n \cdot q_{e^-}) / C$ and $\Delta v = -12 \text{ cm}^{-1}$, we can obtain an estimated number (n) of electrons ~ 150 . This number can be considered as a net difference of transferred electrons due to a tunneling process assisted by a surface plasmon oscillation on the terahertz frequency.¹¹ The estimated number of the tunneled electrons is rather low compared with those molecular junctions with measured current of pA to nA magnitude.^{12,13} This discrepancy might be explained by: 1) in molecular junctions where pA to nA rectified current was observed, a bias voltage (0.1~1.0 V) was usually applied whereas in our case no bias was applied; 2) with a gap size of $\sim 0.9 \text{ nm}$, the conductive channel has not been established so that electrons cannot easily flow across the gap; or 3) the effect of coulomb repulsion increases as the number of tunneled electrons increases (coulomb blockade).

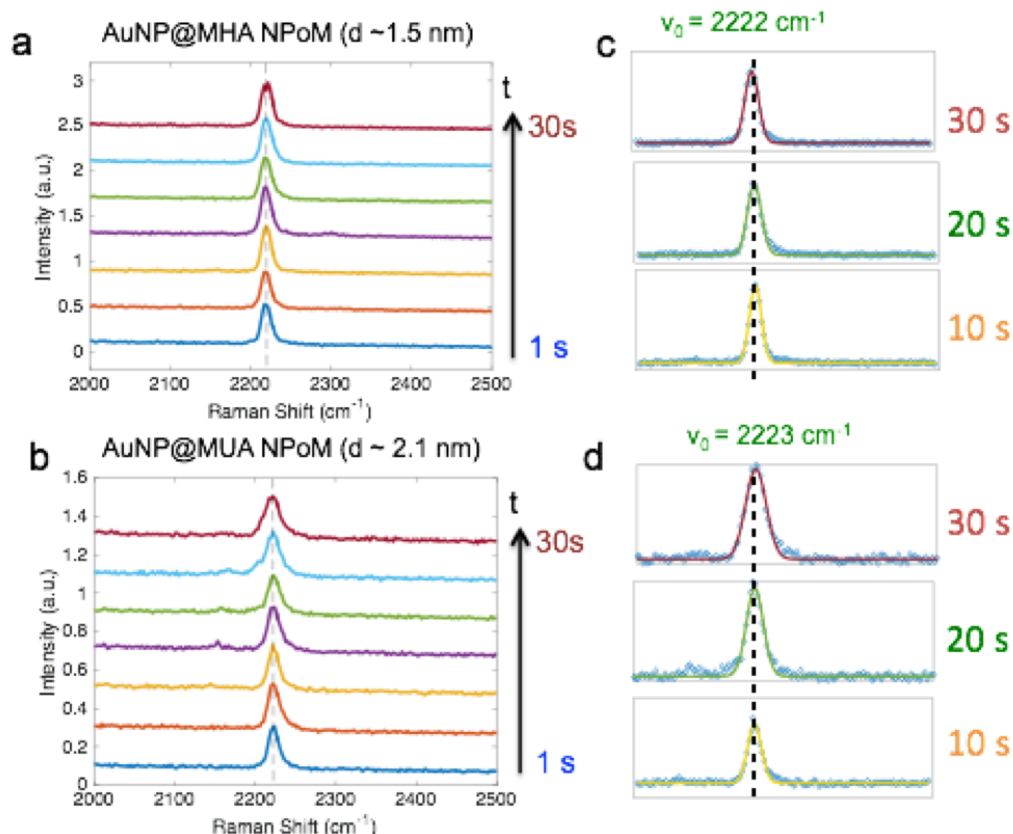


Figure S14. (a, b) SERS spectra selected from the time series (1s, 5s, 10s, 15s, 20s, 25s, 30s) of larger NPoM gaps. (c, d) corresponding peak fits for selected time points. Dotted lines are guides for the eye.

References

- (1) Bain, C. D.; Troughton, E. B.; Tao, Y. T.; Evall, J.; Whitesides, G. M.; Nuzzo, R. G. *Journal of the American Chemical Society* **1989**, *111*, 321.
- (2) Tao, Y. T.; Wu, C. C.; Eu, J. Y.; Lin, W. L.; Wu, K. C.; Chen, C. H. *Langmuir* **1997**, *13*, 4018.
- (3) Whelan, C. M.; Smyth, M. R.; Barnes, C. J. *Langmuir* **1999**, *15*, 116.
- (4) Tan, S. F.; Wu, L.; Yang, J. K.; Bai, P.; Bosman, M.; Nijhuis, C. A. *Science* **2014**, *343*, 1496.
- (5) Hill, R. T.; Mock, J. J.; Hucknall, A.; Wolter, S. D.; Jokerst, N. M.; Smith, D. R.; Chilkoti, A. *ACS Nano* **2012**, *6*, 9237.
- (6) Lee, C.; Yang, W.; Parr, R. G. *Phys Rev B Condens Matter* **1988**, *37*, 785.
- (7) Hay, P. J.; Wadt, W. R. *The Journal of Chemical Physics* **1985**, *82*, 299.
- (8) Chen, S.; Meng, L.-Y.; Shan, H.-Y.; Li, J.-F.; Qian, L.; Williams, C. T.; Yang, Z.-L.; Tian, Z.-Q. *ACS nano* **2015**.
- (9) Fang, Y.; Seong, N. H.; Dlott, D. D. *Science* **2008**, *321*, 388.

- (10) Zhang, H.; Yasutake, Y.; Shichibu, Y.; Teranishi, T.; Majima, Y. *Physical Review B* **2005**, *72*, 205441.
- (11) Li, G. Q.; Shishodia, M. S.; Fainberg, B. D.; Apter, B.; Oren, M.; Nitzan, A.; Ratner, M. A. *Nano Letters* **2012**, *12*, 2228.
- (12) Ward, D. R.; Huser, F.; Pauly, F.; Cuevas, J. C.; Natelson, D. *Nat Nanotechnol* **2010**, *5*, 732.
- (13) Arielly, R.; Ofarim, A.; Noy, G.; Selzer, Y. *Nano Lett* **2011**, *11*, 2968.